A Comparative Study of Surface Energies and Water Adsorption on Ce-Bastnästite, La-Bastnästite, and Calcite via Density Functional Theory and Water Adsorption Calorimetry

Sriram Goverapet Srinivasan[+], *Radha Shivaramaiah*[#], *Paul R. C. Kent*[$,‡], *Andrew G. Stack*[+], *Richard Riman*[‖], *Andre Anderko*[‡], *Alexandra Navrotsky*[#,*], *Vyacheslav S. Bryantsev*[+,*]

[+]Chemical Sciences Division, Oak Ridge National Laboratory, 1 Bethel Valley Road, Oak Ridge, TN 37831, USA

[#]Peter A. Rock Thermochemistry Laboratory and NEAT ORU, University of California Davis, 1 Shields Avenue, Davis, CA 95616, USA

[$]Center for Nanophase Materials Sciences, Oak Ridge National Laboratory, 1 Bethel Valley Road, Oak Ridge, TN 37831, USA

[‡]Computer Science and Mathematics Division, Oak Ridge National Laboratory, 1 Bethel Valley Road, Oak Ridge, TN 37831, USA

[‖]Department of Materials Science and Engineering, Rutgers, The State University of New Jersey, 607 Taylor Road, Piscataway, New Jersey 08855, USA

[‡]OLI Systems, Inc., 240 Cedar Knolls Road, Suite 301, Cedar Knolls, New Jersey 07927, USA

Abstract:

Bastnäsite, a fluoro-carbonate mineral, is the single largest mineral source of light rare earth elements (REE), La, Ce and Nd. Enhancing the efficiency of separation of the mineral from gangue through froth flotation is the first step towards meeting an ever increasing demand for REE. To design and evaluate collector molecules that selectively bind to bastnäsite, a fundamental understanding of the structure and surface properties of bastnäsite is essential. In our earlier work (*J Phys Chem C*, **2016**, 120, 16767), we carried out an extensive study of the structure, surface stability and water adsorption energies of La-bastnäsite. In this work, we make a comparative study of the surface properties of Ce-bastnäsite, La-bastnäsite, and calcite using a combination of density functional theory (DFT) and water adsorption calorimetry. Spin polarized DFT+U calculations show that the exchange interaction between the electrons in Ce *4f* orbitals is negligible and that these orbitals do not participate in bonding with the oxygen atom of the adsorbed water molecule. In agreement with calorimetry, DFT calculations predict larger surface energies and stronger water adsorption energies on Ce-bastnäsite than on La-bastnäsite. The order of stabilities for stoichiometric surfaces is as follows: $[10\bar{1}0] > [10\bar{1}1] > [10\bar{1}2] > [0001] > [11\bar{2}2] > [10\bar{1}4]$ and the most favorable adsorption sites for water molecules are the same as for La-bastnäsite. In agreement with water adsorption calorimetry, at low coverage water molecules are strongly stabilized via coordination to the surface Ce^{3+} ions, whereas at higher coverage they are adsorbed less strongly via hydrogen bonding interaction with the surface anions. Due to similar water adsorption energies on bastnäsite $[10\bar{1}1]$ and calcite $[10\bar{1}4]$ surfaces, the design of collector molecules that selectively bind to bastnäsite over calcite must exploit the structural differences in the predominantly exposed facets of these minerals.

Introduction:

Rare earth elements (REE) that include Y, Sc and the fifteen lanthanides are essential ingredients of phosphors, ceramics, metal alloys, batteries, permanent magnets, and catalysts for petroleum refining and emission control in automobile catalytic converters.[1, 2] Among these, the elements from La to Sm are classified as light rare earths (LREE).[3] Bastnäsite, a fluoro-carbonate mineral of general formula $MFCO_3$ ($M = La^{3+}/Ce^{3+}/Y^{3+}$), is the single largest mineral source of LREE. For example, high grade bastnäsite ore found in Mountain Pass, California, USA contains mostly Ce (> 50 %) and La (> 25 %), with about 12 % Nd and 1.2 % Pr. The first step in the process of extracting REE from the ore is the separation of the mineral from the gangue, referred to as ore beneficiation. The most commonly used beneficiation technique for bastnäsite is froth flotation,[3] which relies on selective adhesion of air bubbles to mineral surfaces in an aqueous slurry based on the difference in the surface hydrophobicity between that of mineral and the gangue. Collector molecules used in froth flotation must selectively bind to the mineral surface over that of the gangue material, rendering the mineral surface hydrophobic. With an ever-increasing demand for REE,[4] design of collector molecules with enhanced selectivity for bastnäsite over gangue is essential to improve the economics of mining REE and maximize REE production.

Owing to their low cost, tall oil fatty acids are commonly used as collector molecules in bastnäsite flotation. However, fatty acids are known to be poorly selective for bastnäsite over calcite gangue and require large amounts of added depressant compounds to achieve the desired concentrate grades/recoveries.[2,5] With the existing mineral processing technology, only ~60 − 65 % of bastnäsite is recovered from high-grade ore containing ~8.5 % bastnäsite, while the rest is lost in tailings.[6,7] It is much more difficult to concentrate low-grade ores containing 1−2 % of the

REE-bearing mineral. However, agents with flotation efficiency improved by 10% or more could shift the paradigm for exploiting potential REE deposits. Although considerable efforts have been devoted to the development of efficient collector molecules,[5,8-14] the design of these molecules has largely been based on trial and error, along with empirical rules of thumb and knowledge gained from floating other minerals. Very little work[15,16] has been done in gaining an atomistically detailed understanding of the bulk and surface structure of the mineral to enable rational design of molecules with high selectivity for bastnäsite. With this objective, in our earlier work,[17] we undertook an extensive study of La-bastnäsite to elucidate its bulk structure, surface stability and water adsorption energies using a combination of density functional theory calculations (DFT), powder X-ray diffraction, and water adsorption calorimetry experiments. We showed that the structure of La-bastnäsite is isomorphic to Ce-bastnäsite, consisting of two bilayers of LaF^{2+} and CO_3^{2-} ions. Among various stoichiometric surfaces, the nonpolar $[10\bar{1}0]$, but, nonetheless, electron rich surface containing layers of $LaFCO_3$ is the most stable, which can be targeted to find adsorbent structures that are complementary to the structure of this surface.

In this work, we have performed a comparative analysis of the bulk structure, surface properties, and water adsorption energies of Ce-bastnäsite, La-bastnäsite, and calcite using DFT calculations and water adsorption calorimetry. While each Ce^{3+} ion in Ce-bastnäsite contains an unpaired electron localized on its *4f* orbital, we show that the exchange interaction between the *f* electrons on different Ce^{3+} sites is negligible. DFT calculations and calorimetric measurements show higher surface energies and more favorable water adsorption energies on Ce-bastnäsite compared to La-bastnäsite surfaces. The structural similarity and order of surface stability of Ce- and La-bastnäsite and their differences from calcite suggests a congruent molecular design strategy for the recognition of Ce- and La-bastnäsite over calcite. Together with our earlier

work[17] on La-bastnäsite, this work lays the necessary foundation to design collector molecules with enhanced selectivity for bastnäsite over calcite gangue.

Computational Methods:

Density functional theory calculations were carried out using the VASP pseudopotential plane wave software.[18-21] The valence states were expanded in a basis of plane waves and the core-valence interactions were described using the Projector Augmented Wave approach (PAW).[22,23] A plane wave kinetic energy of 600 eV was found to be sufficient and thus was used in all the calculations. Indeed, employing a higher plane wave energy cutoff of 800 eV resulted in the negligible changes of the lattice constants (<0.008 Å), $[10\bar{1}0]$ surface energies (< 0.6 meV) and water adsorption energies (0.01−0.15 kJ/mol) on the $[10\bar{1}0]$ surface. Consistent with our earlier work on La-bastnäsite,[17] we used the PBEsol generalized gradient approximation (GGA) functional[24] to describe the exchange correlation interactions and the DFT-D3 method[25] to include the van der Waals' interactions between the CeF^{3+} and CO_3^{2-} groups in Ce-bastnäsite, Ca^{2+} and CO_3^{2-} groups in calcite, and water molecules and the cleaved surfaces. The self-consistent field (SCF) convergence threshold was set to 10^{-5} eV in all the calculations. During the SCF solution, a Pulay mixing scheme[26] was used for charge density mixing. A well-converged Gamma centered $\boldsymbol{k}$-point mesh was used to sample the Brillouin zone for Ce-bastnäsite ($4 \times 4 \times 4$) and calcite ($6 \times 6 \times 2$) bulk calculations. Further increasing the k point mesh had a negligible effect on the cell parameters (<0.001 Å) and the total energies of bulk and slab models (<1 meV). Structural relaxations of $Ce_2O_{3(s)}$, $CeF_{3(s)}$ and $CaO_{(s)}$ were carried out beginning from their experimental crystal structures in the $P\bar{3}m1$[27], $P\bar{3}c1$[28] and $Fm\bar{3}m$[29] space groups, while their Brillouin zones were sampled using a ($8 \times 8 \times 6$), ($4 \times 4 \times 4$) and (12×12

× 12) Gamma centered ***k***-point mesh, respectively. Optimization of $CO_{2(g)}$ and $H_2O_{(g)}$ molecules was carried out in a 15 Å × 15 Å × 15 Å box. Positions of all the atoms were relaxed in our calculations and the geometry was optimized until the forces on all atoms dropped below 0.01 eV/Å.

In Ce-bastnäsite, the Ce ions are present in their +3 oxidation state. As a result, each Ce^{3+} ion contains an unpaired electron in the *4f* orbital. The presence of an unpaired electron on each Ce^{3+} ion gives rise to the possibility of a number of energetically closely lying magnetic states with different spin orientations. To identify the lowest lying magnetic ordering in Ce-bastnäsite, six different configurations with ferromagnetic (FM) and antiferromagnetic (AFM) ordering of spins were considered. Since it is well known that GGA-DFT fails to describe the localized nature of the *'f'* electrons due to large self-interaction error, we have used spin-polarized calculations together with the rotationally invariant DFT+U approach of Dudarev et al.[30] However, the use of a Hubbard U term makes the potential orbital dependent, resulting in multiple self-consistent solutions corresponding to different *'m'* projections of the *4f* orbital on Ce with widely varying energies. In order to identify the lowest electronic state for a given magnetic ordering, we followed the two step procedure suggested by Meredig et al.[31] First, a spin polarized single point calculation at the experimental lattice parameters of Ce-bastnäsite was carried out without the inclusion of the Hubbard U term (i.e. U=0.0 eV). Then, beginning with the wavefunction from the previous step, cell optimization using the spin polarized DFT+U calculations was performed at the desired U value. At the end of each calculation, the magnetic moment on the Ce^{3+} ions was checked to confirm that the SCF solution converged to the desired magnetic state. Three different values of the effective Hubbard U were tested in our calculations, 3.0, 4.5 and 6.0 eV. Our results indicated that at all values of U, the energy difference between

different magnetic ordering of spins in Ce-bastnäsite is less than 1meV per formula unit, pointing to a negligible exchange interaction between the unpaired electrons on different Ce^{3+} ions. Thus, for all subsequent calculations, only the high spin electronic state was considered. In addition to spin polarized DFT+U calculations, we have also carried out non-spin-polarized calculations using a different pseudopotential (PSP) configuration, wherein the Ce *4f* orbitals were included in the core (hereafter called 'large core PSP'). All the calculations on calcite were non-spin-polarized using a Ca PSP with $3s^2 3p^6 4s^2$ valence electronic configuration.

Surface calculations were performed on five different surfaces found in natural crystallites of bastnäsite, namely [$10\bar{1}0$], [0001], [$10\bar{1}1$], [$10\bar{1}2$] and [$11\bar{2}2$] surfaces[32], and the [$10\bar{1}4$] surfaces of Ce-bastnäsite and calcite. Among these, the [$10\bar{1}0$], [$10\bar{1}2$] and [$10\bar{1}4$] surfaces are nonpolar, while the [$10\bar{1}1$], [$11\bar{2}2$] and [0001] surfaces are dipolar. For the dipolar surfaces, half of the surface terminating groups were moved from the top to the bottom end of the slab as a way to minimize the formal dipole moment in the direction perpendicular to the slab. In our earlier work on La-bastnäsite,[17] we had explored a number of different truncations and terminations for each surface and identified the lowest lying structure through a combination of geometry optimizations and DFT molecular dynamics based annealing. In the current work, the initial structures for various surfaces were taken from their lowest lying configuration of La-bastnäsite and the lattice parameters were scaled to match the lattice constants of bulk Ce-bastnäsite. We used a vacuum gap of 20 Å between the adjacent slab images, which is sufficient to obtain converged surface and adsorption energies. Geometry optimizations beginning from these structures were carried out using both spin polarized DFT+U (with U = 4.5 eV) calculations and non-spin-polarized calculations with the large core PSP. Comparison with the experimental data[28] indicates that the lattice parameters are slightly underestimated, with the

percent error of 0.7–1.2%. Taking into account a small expansion of the lattice due to vibrations, the agreement between the computed and experimental lattice parameters is excellent. For dipolar surfaces, the total energies were corrected for dipole and quadrupole interactions in the surface normal direction.[33,34] The surface energy in vacuum was calculated using (1):

$$E_{surf}^{vac} = \frac{E_{slab} - NE_{bulk}}{2A} \qquad (1)$$

where, E_{slab} is the total energy of the slab, E_{bulk} is the total energy of bulk Ce-bastnäsite, N is the number of $CeFCO_3$ formula units in the slab and A is the surface area of the slab. The factor of 2 in the denominator of equation (1) accounts for the presence of two surfaces (top and bottom) in the slab. The surface energies obtained from these calculations were then used to predict the equilibrium shape of a Ce-bastnäsite nanoparticle via thermodynamic Wulff construction[35] using the Wulffman program.[36,37] The Wulff shape was generated by providing the computed surface energies and the space group of the bastnäsite crystal as input to the Wulffman program.

The hydration energy of the surfaces was computed using the large core PSP pseudopotential and an implicit solvent model using VASPsol,[38] (VASPsol is not implemented for DFT+U) with default setting for water (i.e., $\varepsilon = 78.4$, $\sigma = 0.6$, $\tau = 0.525$ meV Å^{-2}).

The solvation energy of the surface is calculated using equation (2):

$$E^{sol} = \frac{E_{slab}^{sol} - E_{slab}}{2A} \qquad (2)$$

where, E_{slab}^{sol} is the total energy of the slab in the presence of an implicit solvent. The total energy of a surface was obtained by summing E^{sol} and E_{surf}^{vac} from equations (1) and (2).

To quantify the structural changes upon the formation of a surface, the minimum, maximum and the mean C-O and Ce-F bond lengths in Ce-bastnäsite and C-O bond lengths in

calcite were computed. The change in the bond lengths ($\Delta_{C\text{-}O}$ and $\Delta_{Ce\text{-}F}$) with respect to the bulk was obtained using equation (3) (shown for the C-O bond)

$$\Delta_{C-O} = \frac{r_{C-O:avg}^{surf} - r_{C-O:avg}^{bulk}}{r_{C-O:avg}^{bulk}} \times 100 \qquad (3)$$

where, $r_{C-O:avg}^{surf}$ is the mean C-O bond length on a surface, $r_{C-O:avg}^{bulk}$ is the mean C-O bond length in the bulk. The variation in the C-O and Ce-F bond lengths within a given structure was computed using equation (4) (shown for the C-O bond)

$$\delta_{C-O} = \frac{r_{C-O}^{max} - r_{C-O}^{min}}{r_{C-O}^{avg}} \times 100 \qquad (4)$$

where, r_{C-O}^{max}, r_{C-O}^{min} and r_{C-O}^{avg} are the maximum, minimum and mean C-O bond lengths in a given structure, respectively.

The adsorption energy of water was calculated using (5)

$$E_{ads}^{n} = \frac{E_{slab}^{nH_2O} - E_{surf} - nE_{H_2O}}{n} \qquad (5)$$

where $E_{slab}^{nH_2O}$ is the energy of the surface with 'n' adsorbed water molecules, E_{H_2O} is the energy of a water molecule in the gas phase. The stabilization energy of successive water molecules on the $[10\bar{1}0]$ surface was calculated using equation (6)

$$E_{stab} = \frac{E_{slab}^{(n+4)H_2O} - E_{slab}^{nH_2O} - 4E_{H_2O}}{4} \qquad (6)$$

where 4 accounts for the presence of 4 Ce^{3+} ions on the surface, two each on either sides of the slab. Molecular graphics in this article were generated using the VESTA software.[39]

Experimental Methods

Synthesis

$CeFCO_3$ was synthesized by urea hydrolysis in the presence of NH_4F as a source of F^-. In a typical synthesis 0.02 mol of $REE(NO_3)_3$ was dissolved in 20 mL of water and was added to a 50 mL of a solution containing 0.02 mol of NH_4F under stirring. After 30 mins, 0.04 mol of urea was added to this mixture and the resulting solution was aged at 90 °C for 20 h. The precipitate was separated by centrifugation, washed with DI water and dried at 60 °C.[40,41] Commercially available high purity calcite was procured from Nanomaterials Technology Co., Singapore.

Characterization

Powder X-ray diffraction patterns (XRD) of both the samples were recorded using a Bruker AXS D8 Advance diffractometer with CuKα radiation, Kα = 1.5418 Å. Data were recorded between 20 and 100 ° 2θ with steps of 0.02 ° and counting time of 10 s per step. Surface area measurement was by the Brunauer−Emmett−Teller (BET) method using a Micromeritics Gemini VII surface area analyzer. The samples were degassed at 150 °C for 10 h before the measurements to obtain the surface area using N_2 adsorption isotherm.

Water adsorption calorimetry

Water adsorption calorimetry was used to measure the surface energy of both $CeFCO_3$ and calcite. In this methodology, we monitor the heat of adsorption of water onto the surface of the sample as a function of surface coverage. This methodology is essentially the same as that used for $LaFCO_3$ in our earlier report[17] and additional experimental details can be found elsewhere.[42,43] Briefly, in a typical experiment a pelletized sample was taken on one side of a silica glass fork tube and was degassed under vacuum for 10 h at 150 °C to remove all the adsorbed water molecules. Then, a coupled Micromeritics ASAP2020 analyzer and a Setaram DSC111 Calvet microcalorimeter operated at 25 °C were used to measure the water adsorption enthalpy on the surface of the sample. During this step, the water vapor was dosed into the fork

tube in incremental values of 1 micromole H_2O per dose using ASAP 2020 analyzer. The amount of adsorbed water vapor on the sample surface in fork tube was determined from the pressure drop (relative pressure P/P_0) as the water vapor is removed from the sample chamber onto the sample surface. Each water dose generates a distinct calorimetric peak due to heat effects associated with water adsorption and the integral of the area under the peak provides the corresponding heat of adsorption (differential enthalpy). The amount of water adsorbed until the differential enthalpy equals the condensation enthalpy (-44 kJ/mol) of water is considered to be chemisorbed. The remaining water adsorbed at -44 kJ/mol is considered to be physisorbed and at this stage, the surface is assumed to be like a liquid and its surface energy is equal to 0.072 J/m^2, as in liquid water. The surface energy of the anhydrous state is then calculated using the equation:

$$0.072 = \gamma_{SG} + \theta \cdot \Delta H_{ads} \quad (7)$$

Here, θ is the minimal water coverage, where the liquid-like state is observed and γ_{SG} is the surface energy of the anhydrous surface. Further details regarding the use of water adsorption for calculating surface energy can be found elsewhere.[42,43] In order to determine the experimental uncertainties, the experiment was repeated twice by degassing the sample at 150 °C for 10 h. In all this work the reference state for water is the vapor, whose enthalpy does not depend on the pressure at a constant temperature since H_2O can be considered an ideal gas at these low pressures. A blank with an empty tube was run to correct the data for water adsorbed on the fork tube wall.

Results and Discussion:

Bulk Structure and Properties:

Ce-bastnäsite has a hexagonal structure ($P\bar{6}2c$ space group) consisting of two alternate layers of three CeF^{2+} and three CO_3^{2-} groups (Figure 1).[28,40] The anions in adjacent layers are rotated by 120° about the *'c'* axis in order to minimize the repulsion between the CO_3^{2-} groups.

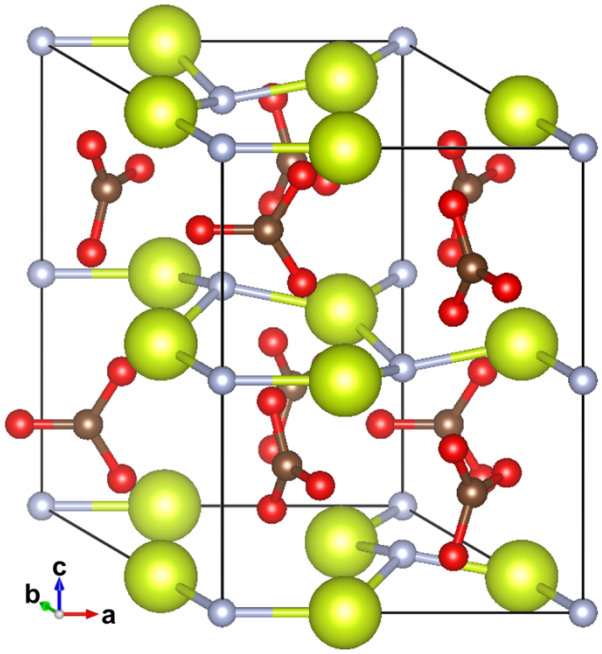

Figure 1: Bulk structure of Ce-bastnäsite. Ce atoms are yellow, C atoms are brown, O atoms are red and F atoms are blue.

The Ce ions are present in their +3 oxidation state, with one unpaired electron localized in the *4f* orbital. The presence of an unpaired electron at the metal ion site could result in a number of different magnetic orderings in the crystal. In order to identify the magnitude of electron exchange interactions, we have considered six different arrangements of spins in ferromagnetic (FM) and antiferromagnetic (AFM) configurations. The layered structure of Ce-bastnäsite allows for AFM ordering of spins within a cationic plane (intra-layer AFM), as well as across cationic layers (inter-layer AFM). Since the unit cell of Ce-bastnäsite contains three metal ions per cationic layer, in order to study intra-layer AFM configurations we considered a ($2 \times 1 \times 1$) supercell of Ce-bastnäsite containing six metal ions per cationic layer. Three different

arrangements of spins within a cationic layer were considered; one FM (Figure 2a) and two AFM arrangements with alternating three rows (Figure 2b) and one row (Figure 2c) of ferromagnetically ordered spins. For every arrangement of spins within a CeF^{2+} layer, two different arrangements of spin across the cationic layers were considered (FM and AFM stacking), resulting in a total of six different magnetic configurations.

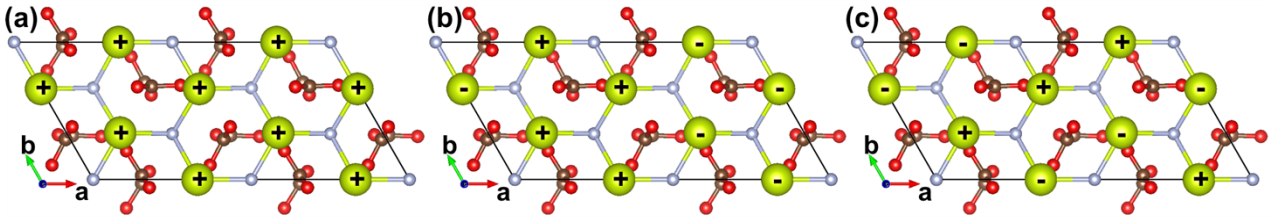

Figure 2: Intra-layer magnetic configurations in the cation plane of Ce-bastnäsite. For every configuration, two different inter-layer spin arrangements, corresponding to FM and AFM stacking were considered. Ce atoms are yellow, C atoms are brown, O atoms are red and F atoms are blue. '+' denotes up spin electrons while '-' denotes down spin electrons.

Cell optimizations beginning from the experimental lattice parameters were carried out for all six magnetic arrangements using spin polarized DFT+U calculations with three different values of U, namely 3.0, 4.5, and 6.0 eV. In all cases, the energy difference between any two magnetic states was less than 1meV per formula unit, indicating negligible exchange interactions between the unpaired electrons on different Ce^{3+} ions. Thus, for all subsequent calculations, we consider only the ferromagnetic electronic state with each Ce^{3+} ion having a magnetization of $1\mu_B$.

Table 1 gives the optimized lattice parameters, formation energies and GGA-DFT band gaps of Ce-bastnäsite and calcite together with the available experimental values. The formation energies of Ce-bastnäsite and calcite were computed via reactions (8) and (9), respectively:

$1/3\ Ce_2O_{3(s)} + 1/3\ CeF_{3(s)} + CO_{2(g)} \rightarrow CeFCO_{3(s)}$ (8)

$CaO_{(s)} + CO_{2(g)} \rightarrow CaCO_{3(s)}$ (9)

Table 1: Lattice parameters, formation energies, and electronic band gaps of Ce-bastnäsite and calcite. All the calculations used the PBEsol GGA functional and the 600 eV plane wave kinetic energy cutoff. The Brillouin zones of Ce-bastnäsite (4x4x4) and calcite (6x6x2) were sampled using a Gamma centered ***k***-point mesh.

Method	*a* (Å)	*c* (Å)	ΔE_f (KJ/mol)	Band Gap (eV)
Ce-bastnäsite				
f-in-core	7.067	9.742	-179.3	4.66
U = 3.0 eV	7.045	9.731	-204.5	2.64
U = 4.5 eV	7.060	9.737	-224.8	3.81
U = 6.0 eV	7.074	9.745	-250.8	4.53
Expt. values	7.144[28]	9.808[28]	-141.2[41]	-
Calcite				
GGA-DFT	4.993	16.700	-186.3	5.01
Expt. values	4.990[44]	17.061[44]	-178.3[45]	6.0 $\pm$ 0.35[46]

The results of calculations indicate that the lattice parameters and formation energies of calcite are in very good agreement with their experimental values, while the GGA-DFT band gap is underestimated by *ca.* 1 eV. Similarly, the lattice parameters of Ce-bastnäsite predicted by all the methods agree to within 2 % of the experimental values. However, a much larger variation in the band gaps and formation energies of Ce-bastnäsite are observed for different U. It is well known that while the structural properties of a material are less sensitive to the choice of U, the electronic and thermophysical properties are strongly dependent on the value of U.[47] In the absence of any photoemission spectra data to compare against our predicted electronic density of states, the optimal value of U for Ce-bastnäsite is unknown. Fabris et al.[48] used a linear response approach to determine self-consistently a value of U = 4.5 eV for the Ce *4f* orbitals in ceria, which has been used extensively to study catalysis on ceria surfaces. In line with earlier works,[49-51] we have used a value of U = 4.5 eV in the subsequent surface calculations and have compared

the results with the pseudo-singlet state calculations, wherein the *4f* orbitals are included in the core.

Figure 3 shows the electronic structure of Ce-bastnäsite computed at the DFT+U level (U = 4.5 eV). The occupied *4f* orbitals on the Ce^{3+} ions can be seen as split-off states right below the Fermi level. Both the valence and conduction band edges of Ce-bastnäsite consist predominantly of Ce 4*f* orbitals. Ce-bastnäsite has a relatively flat band structure with a GGA band gap of 3.81 eV, suggesting highly ionic character of the Ce−O and Ce−F bonds.

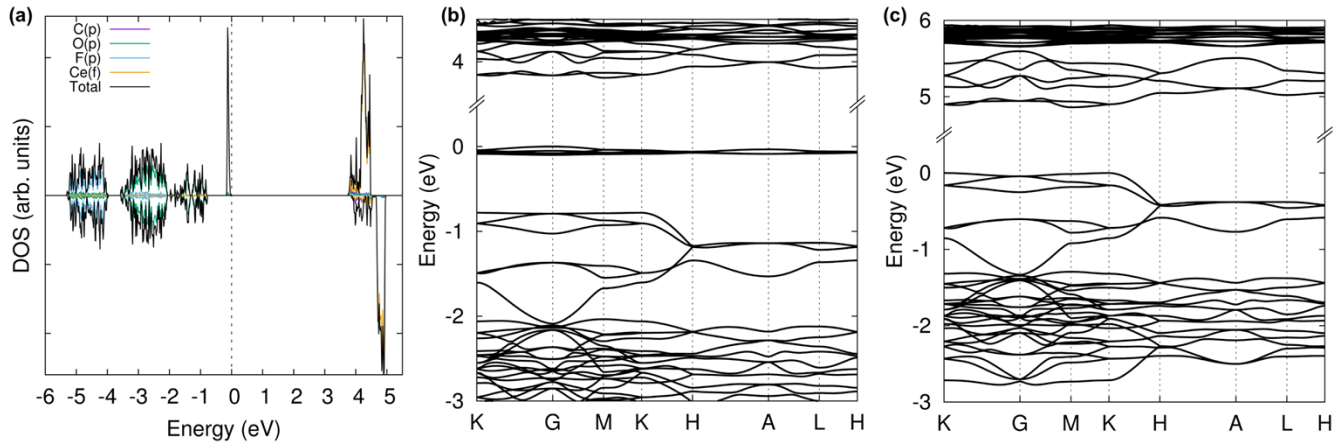

Figure 3: Electronic structure of Ce-bastnäsite. (a) Electronic density of states, (b) majority spin band structure, and (c) minority spin band structure. The Fermi level is set to 0 eV in panel (a), while the valence band maximum is set to 0 eV in panels (b) and (c).

Surface structures and energies:

We have studied six different surfaces commonly exposed in natural crystals of Ce-bastnäsite, namely [10$\bar{1}$0], [0001], [10$\bar{1}$1], [10$\bar{1}$2], [10$\bar{1}$4] and [11$\bar{2}$2].[32] Among these, the [10$\bar{1}$0], [10$\bar{1}$2] and [10$\bar{1}$4] surfaces are nonpolar, while the other three surfaces, [0001], [10$\bar{1}$1] and [11$\bar{2}$2], are dipolar. Atomic structures of the cleaved and fully relaxed surfaces in the gas phase are given in Electronic Supplementary Information (ESI). Optimized structures of all studied

surfaces with an adsorbed water molecule are shown in Figure 4. Table 2 presents the mean, minimum and maximum C-O and Ce-F bond lengths of various Ce-bastnäsite and calcite surfaces along with the variations in the bond lengths computed using the full valence PSP for Ce, while Table S1 of the ESI presents the corresponding values obtained using the large core PSP. Table 3 summarizes the surface energies (E_{surf}^{vac}) and hydration energies (E^{sol}) of Ce-bastnäsite that are compared with the corresponding values for La-bastnäsite reported earlier,[17] while Table 4 presents the surfaces energies and hydration energies for the most stable calcite [10 $\bar{1}$4] surface.

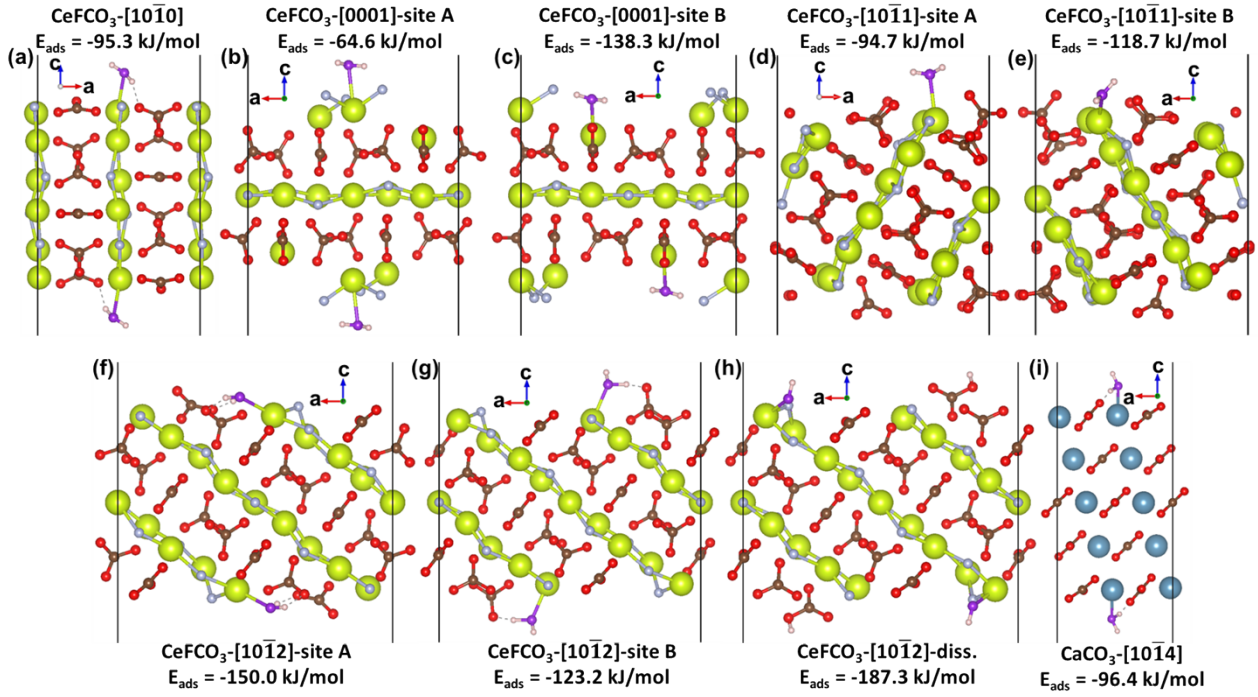

Figure 4: Optimized structure of a water molecule adsorbed on various Ce-bastnäsite and [10$\bar{1}$4] calcite surfaces. Ce atoms are yellow, Ca atoms are blue, F atoms are silver, C atoms are brown, O atoms are red, O atoms in water are purple and H atoms white.

Among the nonpolar surfaces, our analysis reveals that [10$\bar{1}$0] can be cleaved in two different ways depending on the orientation of the CO_3^{2-} groups at the surface, while the [10$\bar{1}$2]

and [10$\bar{1}$4] surfaces can be cleaved in one way only. Similar to La-bastnäsite, upon structural relaxation, there is only a slight reorientation of the surface CO_3^{2-} groups and relatively small changes in subsurface atom positions, resulting in [10$\bar{1}$0] being the most stable Ce-bastnäsite surface with a surface energy of *ca.* 0.8 J/m^2 in vacuum and *ca.* 0.48 J/m^2 in the presence of an implicit solvent. The [10$\bar{1}$2] and [10$\bar{1}$4] surfaces are stepped surfaces having alternate layers of CeF^{2+} and CO_3^{2-} groups that are oriented at an angle of 51.4 ° and 68.2 °, respectively, from surface normal. While the changes in the orientation of the CO_3^{2-} groups at the surfaces are largely similar between La and Ce-bastnäsite surfaces, the changes in the mean C−O and M−F (M = Ce/La) bond lengths with respect to the bulk are larger for Ce- than for La-bastnäsite. With the largest variation in the C−O and Ce−F bond lengths within the structure, the [10$\bar{1}$4] surface is the least stable surfaces studied in this work.

For the dipolar surfaces, we considered a (2 × 1 × 1) expansion of the Ce-bastnäsite surface unit cell and moved half of the surface terminating groups from one end of the slab to the other end to nullify the dipole moment along the surface normal direction. It must be noted that dipolar oxide surfaces are known to undergo complex surface reconstructions in order to minimize the dipole moment in the surface normal direction.[52] However, to the best of our knowledge, no experimental data on surface reconstructions of bastnäsite is currently available. Each of these surfaces can be cleaved in more than one way to obtain different stoichiometric surface terminations. For instance, the [0001] surface can be terminated either by the CO_3^{2-} or the CeF^{2+} groups. Similarly, the [10$\bar{1}$1] surface can have five different terminations, namely F^-, Ce^{3+}, CO_3^{2-}, CeF^{2+} and $LaFCO_3$. In our earlier work on La-bastnäsite,[17] we undertook an extensive study of all possible surface cuts and terminations for each of the three dipolar surfaces. For example, we considered 16 and 9 different configurations for the CO_3^{2-} and LaF^{2+}

terminated [0001] surfaces based on the constraint that the resulting structure has elements of symmetry, while 24 different initial configurations were considered for the $[10\bar{1}1]$ surface, representing various terminations. In the present work, we consider only those surface terminations for Ce-bastnäsite that were identified to be the most stable configurations for La-bastnäsite. The geometrical changes upon optimization of these structures are very similar to those observed for La-bastnäsite. Specifically, we see a significant reorientation of the CO_3^{2-} groups on the [0001]- CO_3^{2-} surface that were initially directed normal to the surface and the movement of a surface Ce^{3+} ion to the subsurface CO_3^{2-} layer on the [0001]-CeF^{2+} surface. Due to more compact arrangement of the atoms on $[10\bar{1}1]$-CO_3^{2-} and $[11\bar{2}2]$ surfaces, structural relaxation resulted only in small changes in the atomic positions compared to bulk (Table 2).

As follows from Table 3, the surface energy of all the Ce-bastnäsite surfaces are larger than those of La-bastnäsite surfaces, which is consistent with breaking stronger ionic bonds (as seen from shorter bond distances) in Ce-bastnäsite compared to La-bastnäsite upon surface formation. The relative order of stability remains the same between Ce and La-bastnäsite surfaces, viz. $[10\bar{1}0] > [10\bar{1}1] > [10\bar{1}2] > [0001] > [11\bar{2}2] > [10\bar{1}4]$. Furthermore, in all cases, the surface energies computed using the full valence PSP for Ce and spin polarized DFT+U (U = 4.5 eV) are consistent with the results obtained using the large core PSP, the latter being systematically larger by $0.02 - 0.06$ J/m^2. The hydration energies of Ce-bastnäsite surfaces are, as expected, more exothermic than those of La-bastnäsite surfaces, consistent with the smaller ionic radius[53] (1.216 Å (La^{3+}) and 1.196 Å (Ce^{3+}) for the coordination number 9) and larger hydration enthalpy[54] (-3312 kJ/mol (La^{3+}) and -3367 kJ/mol (Ce^{3+})) of Ce^{3+} compared to La^{3+}.

Figure 5 shows the equilibrium shape of a Ce-bastnäsite nanoparticle predicted via thermodynamic Wulff construction based on the computed surface energies. Similar to La-

bastnäsite, the Ce-bastnäsite nanoparticle is predicted to have a hexagonal prism morphology, consisting of [10$\bar{1}$0] side and [0001] base terminations chiseled at its edges by the [10$\bar{1}$1] and [10$\bar{1}$2] terminations. This agrees well with the morphology of natural crystals[55], except that the basal plane is exhibited more frequently in the experimental samples. We are currently investigating possible reaction of water and CO_2 with surface atoms and the role of nonstoichiometric terminations in stabilizing the dipolar [0001] surface. The area weighted average surface energy of the nanoparticle computed using the small (large) core PSP is 0.89 (0.93) J/m^2, which is 0.03 (0.07) J/m^2 larger than that of La-bastnäsite. This value can be compared to the surface energy of synthetic Ce-bastnäsite, 1.3 ± 0.1 J/m^2 measured by adsorption calorimetry, which is larger than the experimental value for La-bastnäsite, 1.1 ± 0.1 J/m^2.

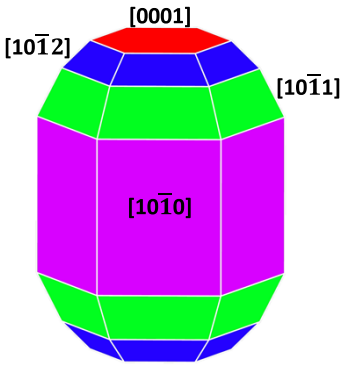

Figure 5: Ce-bastnäsite nanoparticle shape predicted by thermodynamic Wulff construction. Surface energies were taken from the calculations using the full valence pseudopotential for Ce.

Since calcite is one of the most common gangue minerals present in bastnäsite deposits, it is important to understand and exploit structural and energetic differences between bastnäsite and calcite. The nonpolar calcite [10$\bar{1}$4] surface consisting of layers of $CaCO_3$ is known to be the most stable termination, which largely dominates the calcite morphology. Figure S1 of the ESI

section shows the optimized structure of calcite [$10\bar{1}4$], overlaid with atoms from the cleaved surface. The surface atoms undergo minimal relaxation, as evidenced by the mean C−O bond length that changes by a mere 0.02% (Δ_{C-O}) with respect to its bulk value (Table 2). A larger variation of 3.06 % (δ_{C-O}) in the C−O bond lengths occurs within the structure due to changes in the C−O distances of the surface carbonates. A small relaxation of the structure upon surface formation is in line with its small surface energy (0.59 J/m^2), which is 0.15 – 0.20 J/m^2 lower than that of the most stable Ce-bastnäsite [$10\bar{1}0$] termination. This value of the surface energy is in good agreement with previous theoretical calculations (0.60 J/m^2).[56]

Water Adsorption on Ce-Bastnäsite and Calcite [$10\bar{1}4$] Surfaces:

The adsorption energy of a water molecule was computed for each of the four facets that were exposed in the predicted Wullf structure. For the most stable [$10\bar{1}0$] surface, we have also computed the adsorption energy of water molecules as a function of surface coverage, ranging from 1 (2.91 H_2O/nm^2) to 3 (8.72 H_2O/nm^2) water molecules per surface metal ion. Among the surfaces exposed, the [$10\bar{1}0$], [$10\bar{1}2$] and [0001] surfaces are symmetric while the [$10\bar{1}1$] surface has C_1 symmetry. Thus, for the [$10\bar{1}0$], [$10\bar{1}2$] and [0001] surfaces, water molecules were added symmetrically to the top and bottom ends of the slab. For the [$10\bar{1}1$] surface, a water molecule was added on one side of the slab only. Furthermore, since the metal ions on the [$10\bar{1}1$], [$10\bar{1}2$] and [0001] surfaces are inequivalent, the adsorption of a water molecule on two different surface ions was considered.

Figure 4 shows the optimized structures of a water molecule in the associated state adsorbed on the Ce-bastnäsite [$10\bar{1}0$], [$10\bar{1}1$], [$10\bar{1}2$], and [0001], and calcite [$10\bar{1}4$] surface. For the [$10\bar{1}2$] surface, a water molecule in its dissociated state (an OH^- group bound to the surface metal ion site and a proton attached to the surface carbonate group) is also considered.

Table 5 compares the adsorption energies and the M−O_w (M = Ce^{3+}/La^{3+}/Ca^{2+}) distances to the water oxygen atom for Ce- and La-bastnäsite computed using non-spin-polarized calculations with the larger core PSP.

Table 5: Adsorption energy of a water molecule and M-O_w (M = Ce^{3+}/La^{3+}/Ca^{2+}) distances on bastnäsite and calcite surfaces. All the calculations on Ce-bastnäsite used the large core pseudopotential.

Surface	Adsorption Energy (kJ/mol)		M-O_w distance (Å)	
	Bastnäsite			
	$CeFCO_3$	$LaFCO_3$[a]	$CeFCO_3$	$LaFCO_3$[a]
$[10\bar{1}0]$	-95.3	-89.0	2.56	2.59
$[10\bar{1}1]$-site A	-94.7	-87.9	2.53	2.55
$[10\bar{1}1]$-site B	-118.7	-109.6[b]	2.57	2.60[b]
$[10\bar{1}2]$-site A	-150.0	-141.9	2.51	2.53
$[10\bar{1}2]$-site A, dissociated H_2O	-187.3	-168.4[b]	2.43	2.42[b]
$[10\bar{1}2]$-site B	-123.2	-115.4	2.38	2.35
[0001]-MF^{2+}-site A	-64.6	-56.9	2.62	2.66
[0001]-MF^{2+}-site B	-138.3	-125.9	2.49	2.52
Calcite				
$[10\bar{1}4]$	-96.4		2.37	

[a]Values taken from Ref 17.
[b]Values taken from Ref 17 using the corrected reference state of the clean surface.

In most cases, the M-O_w bond length is shorter and the water adsorption energy is more exothermic for Ce-bastnäsite compared to La-bastnäsite, which is in accordance with the smaller ionic radius of Ce^{3+} versus La^{3+}. One anomaly is a longer Ce-O_w bond at site B on the $[10\bar{1}2]$ surface, despite having the stronger adsorption energy compared to that of La-bastnäsite. This anomaly can be understood by considering the partial dissociation of the adsorbed water on Ce- and La-bastnäsite, with the H-O_w bond length of 1.21 Å and 1.16 Å, respectively. The shorter La-O_w bond is the result of a stronger anionic character of the OH group at site B on the $[10\bar{1}2]$ surface of La-bastnäsite that can interact more strongly with the metal ion.

In general, by replacing La with Ce, the relative affinity of different binding sites remains largely unchanged. The site A of the $[10\bar{1}2]$ surface is the most reactive binding site among the various adsorption sites studied in this work. In addition to the dissociated state with an adsorption energy of -187.3 kJ/mol, we were also able to locate the associated state with an adsorption energy of -150.0 kJ/mol. The presence of a strongly undercoordinated Ce^{3+} ion on the surface (four broken bonds) and the additional stabilization arising from hydrogen bonding interaction with the surface CO_3^{2-} groups are the contributing factors to the high computed water adsorption energies on the $[10\bar{1}2]$ surface. On the other hand, site A on the [0001] surface is the least favorable sites for water adsorption, because the presence of electron rich F^- ions above the plane of the Ce^{3+} ion (Figure 4b) diminishes the interaction with the surface Ce^{3+} cation.

It is instructive to decompose the total adsorption energy of a water molecule into three parts: (i) the deformation of the surface upon binding (dE_{surf}), (ii) the deformation of a water molecule upon binding (dE_{H_2O}), and (iii) the interaction energy between the deformed surface and water (E_{int}). Table 6 summarizes these contributions for various Ce-bastnäsite surfaces and the calcite $[10\bar{1}4]$ surface.

Table 6: Contribution to the total adsorption energy of a water molecule on Ce-bastnäsite and calcite surfaces computed by the distortion/interaction model. All the calculations on Ce-bastnäsite used the large core pseudopotential.

Surface	dE_{surf} (kJ/mol)	dE_{H_2O}(kJ/mol)	E_{int} (kJ/mol)	E_{ads} (kJ/mol)
Ce-bastnäsite				
$[10\bar{1}0]$	6.7	3.2	-105.2	-95.3
$[10\bar{1}1]$-site A	4.2	1.6	-100.5	-94.7
$[10\bar{1}1]$-site B	15.4	2.4	-136.5	-118.7
$[10\bar{1}2]$-site A	40.5	4.2	-194.7	-150.0
$[10\bar{1}2]$-site B	73.7	59.1	-256.0	-123.2
[0001]-CeF^{2+}-site A	12.0	1.3	-77.9	-64.6
[0001]-CeF^{2+}-site B	20.0	4.6	-162.9	-138.3
calcite				
$[10\bar{1}4]$	10.7	7.2	-114.3	-96.4

One can see that in general higher interaction energy translates into higher adsorption energy, which is often associated with larger deformation penalty of the surface. In comparison, the deformation penalty of the water molecule is much smaller, which is only very weakly dependent on the specific adsorption site, except for the partial dissociation at site B on the $[10\bar{1}2]$ surface. For instance, adsorption of a water molecule is more favorable by *ca.* 55 kJ/mol at site A of the $[10\bar{1}2]$ surface compared to the $[10\bar{1}0]$ surface, but the distortion penalty associated with the water molecule is only 1 kJ/mol larger on the $[10\bar{1}2]$ surface. Thus, the major contribution to the difference in the adsorption energy arises from the difference in the interaction energy (90 kJ/mol) and the surface deformation energy (35 kJ/mol).

For the dominant $[10\bar{1}0]$ facet in the Wulff shape, water adsorption and stabilization energies were computed as a function of surface coverage ranging from half to three water molecules per surface metal ion using both spin-polarized DFT+U (U = 4.5 eV) and non-spin-polarized calculations with the large core PSP. Figure 6 shows the optimized structures of a monolayer of water molecules on the calcite $[10\bar{1}4]$ surface and one to three monolayers of

water molecules on the most stable Ce-bastnäsite [10$\bar{1}$0] surface. The interfacial profile of the first water layer on the calcite [10$\bar{1}$4] surface is consistent with high-resolution specular X-ray reflectivity data.[57] An extensive study of various adsorption configurations of water molecules on the [10$\bar{1}$0] surface was carried out in our earlier work on La-bastnäsite.[17] Thus, in the present work, we have only considered the most stable arrangement of water molecules identified for each coverage. Table 7 presents the adsorption and stabilization energies of water molecules and the Ce^{3+}-O_w bond lengths computed using the large core and full valence PSPs. The adsorption energy of water molecules is found to be higher on the Ce-bastnäsite [10$\bar{1}$0] surface as compared to the La-bastnäsite [10$\bar{1}$0] surface, consistent with the higher hydration enthalpy and smaller ionic radius of Ce^{3+} ions. Successive water molecules on the surface are stabilized by hydrogen bonds between themselves and to the surface F^- and CO_3^{2-} ions.

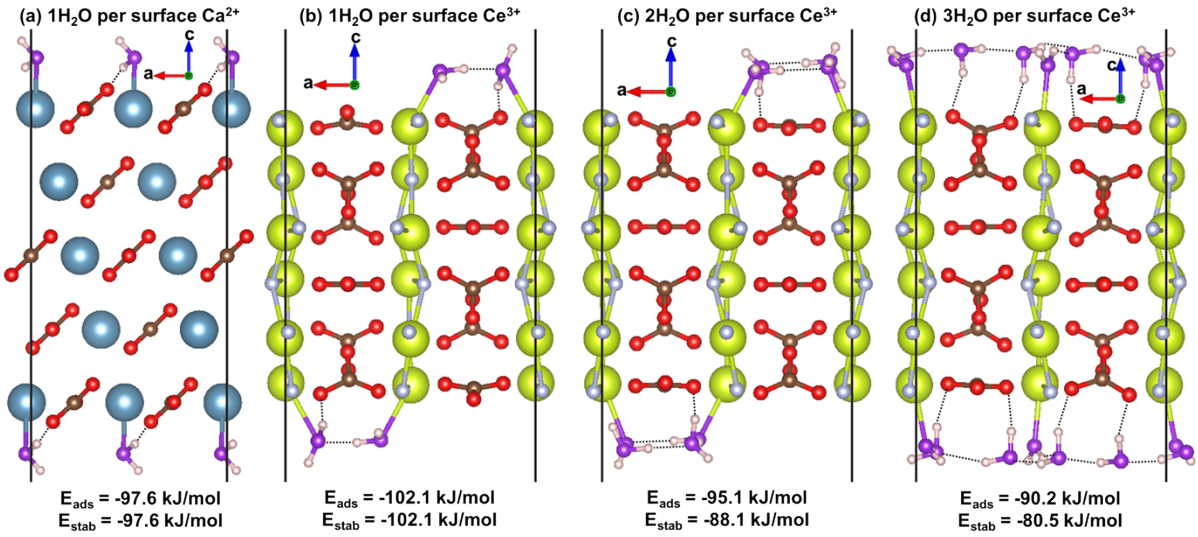

Figure 6: Optimized structure of (a) 1 water molecule per surface Ca^{2+} ion on calcite [10$\bar{1}$4] surface, (b) 1 water, (c) 2 water, (d) 3 water molecules per surface Ce^{3+} ion on Ce-bastnäsite [10 $\bar{1}$0] surface. Ce atoms are yellow, Ca atoms are blue, F atoms are silver, C atoms are brown, O atoms are red, O atoms in water are purple and H atoms white. Calculations on Ce-bastnäsite surfaces used the full valence pseudopotential.

Table 7: Predicted adsorption and stabilization energies and Ce^{3+}-O_w bond lengths as a function of surface coverage on the Ce-bastnäsite [$10\bar{1}0$] surface.

Coverage (H_2O/nm^2)	E_{ads} (kJ/mol)		E_{stab} (kJ/mol)		Ce O_w distance (Å)	
	f-in-core	*f*-in-valence	*f*-in-core	*f*-in-valence	*f*-in-core	*f*-in-valence
2.91	-103.5	-102.1	-103.5	-102.1	2.53, 2.64	2.53, 2.65
5.82	-98.1	-95.1	-92.7	-88.1	2.52, 2.57	2.51, 2.56
8.73	-91.0	-90.2	-76.7	-80.5	2.46, 2.47	2.46, 2.47

Furthermore, we notice that the adsorption energies and the Ce^{3+}-O_w bond distances are fairly insensitive to the choice of the PSP, which can be attributed to the negligible participation of Ce *4f* orbitals in bonding. Indeed, the electronic density of states for a water molecule adsorbed on the Ce-bastnäsite [$10\bar{1}0$] surface shown in Figure 7 indicates that there is no overlap between the Ce '*4f*' states and the '*2p*' states of the water oxygen atoms, which justifies the choice of the large core PSP to compute water adsorption energies. This is consistent with earlier studies on the molecular complexes of lanthanides that showed negligible contribution of the metal *4f* orbital to the metal-ligand bonds.[58] The adsorption energy of a monolayer of water molecules on the most stable calcite [$10\bar{1}4$] surface is -97.6 kJ/mol, in good agreement with earlier reported values (−87.8[59] to −96.1 kJ/mol). This almost equals to the adsorption energy of a water molecule on the La-bastnäsite [$10\bar{1}0$] surface and only 4.5 kJ/mol smaller than the respective value on the Ce-bastnäsite [$10\bar{1}0$] surface.

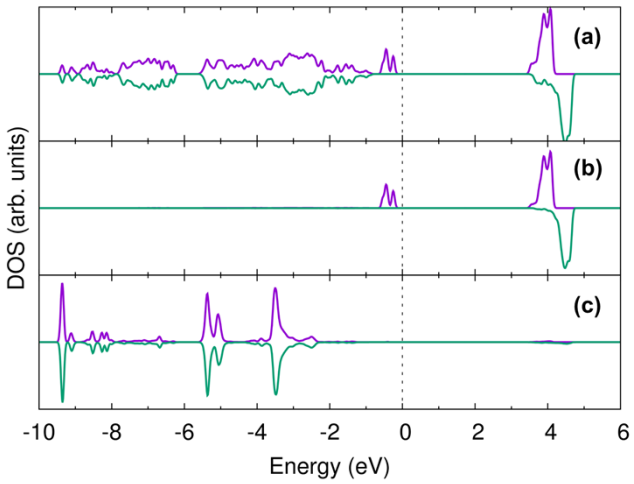

Figure 7: Electronic density of states for a water molecule adsorbed on the Ce-bastnäsite [$10\bar{1}0$] surface. (a) Total density of states, (b) projected density of Ce '*4f*' states, and (c) projected density of O '*2p*' states from the water oxygen. In all the panels, purple line corresponds to the density of spin up states, while the green line corresponds to the density of spin down states. The Fermi level is set to 0 eV.

Water Adsorption Calorimetry:

A typical adsorption isotherm for water on $CeFCO_3$ and the corresponding calorimetric peaks are shown in ESI. Differential enthalpies of adsorption were calculated by taking the integral value of calorimetric peaks and the amount of water adsorbed using the isotherm. Figure 8 shows the differential enthalpies of water adsorption as a function of surface coverage for both $CeFCO_3$ and $CaCO_3$. In both cases, there is a strong initial chemisorption of water on the surface with a differential enthalpy of adsorption of -167.5 ± 4.5 and -148.5 ± 12.1 kJ/mol for the first dose at near zero coverage. The differential enthalpy value becomes less exothermic with successive doses and with increasing surface coverage suggesting that there are more energetically different sites available for the chemisorption of water on the surface of $CeFCO_3$ and $CaCO_3$. Eventually, the differential enthalpy reaches the value of enthalpy of condensation

of bulk water at 25 °C (−44 kJ/mol) in about 8 - 10 doses in both cases as seen in Figure 8. The water adsorbed up to this coverage is strongly bound and is considered to be chemisorbed.

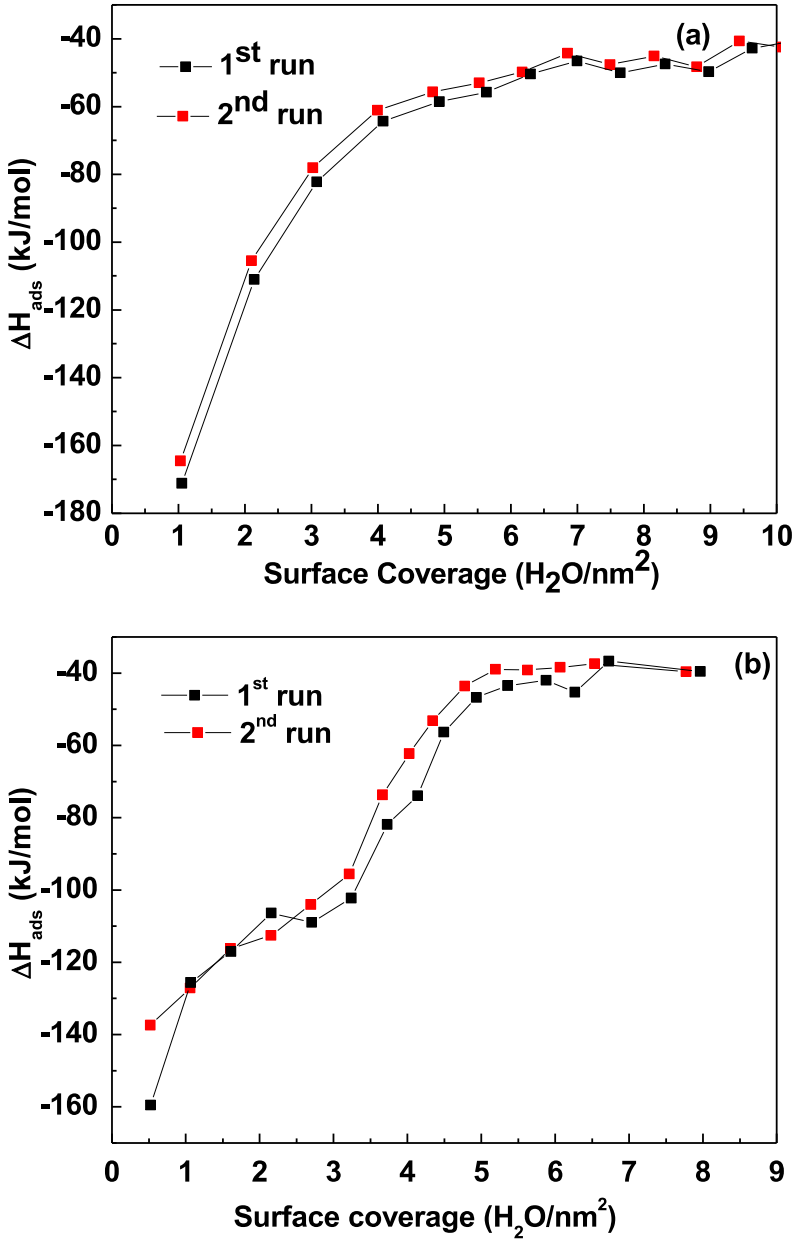

Figure 8. Differential enthalpies of water adsorption as a function of surface coverage for (a) $CeFCO_3$ and (b) $CaCO_3$.

The average water coverage value at this point was 8.98 and 5.36 H_2O/nm^2 on $CeFCO_3$ and calcite surfaces, respectively. The remaining water, with a differential enthalpy of -44 kJ/mol, can be treated as physisorbed water. A summary of water adsorption calorimetry data of $CeFCO_3$ along with $CaCO_3$ and $LaFCO_3$ is given in Table 8. The initial large differential enthalpies in all the three cases suggest a dissociative adsorption of water molecules on the coordinatively unsaturated surfaces. The values for $LaFCO_3$ and $CeFCO_3$ are in good agreement with the highest adsorption energy of the first water molecule bound on the $[10\bar{1}2]$ surface in the dissociated state (Table 5). The ones at later coverage correspond to the water adsorption on different surfaces, which are energetically distinct. The integral enthalpy of adsorption, which corresponds to the enthalpy of chemisorbed water is -79.4 ± 0.98, -96.26 ± 0.96 and -71.6 ± 1.2 kJ/mol for $CeFCO_3$, $CaCO_3$ and $LaFCO_3$ respectively. The computed water adsorption energies for the most stable surface of $CeFCO_3$ (-95.3 kJ/mol), $CaCO_3$ (-96.3 kJ/mol) and $LaFCO_3$ (-89.0 kJ/mol) match our experimental data reasonably well, both in terms of the trend and the values. The surface energies calculated from the water adsorption data using the equation (7) are tabulated in the last column of Table 8. Surface energy of synthetic $CeFCO_3$, $LaFCO_3$ and $CaCO_3$ were found to be 1.3 ± 0.1, 1.1 ± 0.1 and 1.0 ± 0.05 J/m^2 respectively for the anhydrous surface. Measured surface energies once again match calculated surface energies well in terms of the trend, while in terms of the number are a bit higher. Generally, calculated surface values and those obtained from the experiment are seen to agree within 10 – 50 % in the literature.[61] The reasons for this somewhat higher experimental surface energy could be attributed to (i) the GGA-DFT approximation that tends to yield lower interaction energies for ionic compounds and (ii) complexity of real surfaces like different morphology, which could be disordered or amorphous

and thus may expose highly reactive edge sites, kink sites, and grain boundaries as opposed to idealized planar surfaces in the calculations.

Table 8. Water adsorption calorimetry data for $CeFCO_3$, $CaCO_3$, and $LaFCO_3$

Sample	Surface area (m^2/g)	ΔH_{diff} for the first dose of water (kJ/mol)	ΔH_{int} of adsorption of water (kJ/mol H_2O)	Coverage H_2O/nm^2	Surface energy (J/m^2)	
					Experimental	Calculated
$CeFCO_3$	21.50	-171.17	-79.42 ± 0.98	8.98	1.3 ± 0.1	0.89[b];0.93[c]
Calcite	22.41	-159.55	-96.26 ± 0.96	5.36	1.0 ± 0.05	0.60[d]
$LaFCO_3$[a]	67.13	-163.22	-71.6 ± 1.2	9.69	1.1 ± 0.1	0.86

[a]Values for $LaFCO_3$ were taken from previously published data.[17]

[b]F-in-valence calculations for a particle predicted by thermodynamic Wulff construction.

[c]F-in-core calculations for a particle predicted by thermodynamic Wulff construction.

[d]Calculations were performed only for the dominant calcite $[10\bar{1}4]$ surface.

A plot of the measured surface energy of $CeFCO_3$ as a function of the relative pressure of water vapor and amount of water adsorbed is shown in Figure 9. As expected the surface energy values decrease with hydration and decay rapidly with the increasing coverage and eventually approach surface energy of bulk water (0.072 J/m^2). The surface energy of $CeFCO_3$ reaches the bulk water value at relative pressures of 0.28 – 0.4 with ~ 12.5 H_2O/nm^2 whereas for $CaCO_3$ at 0.09 with ~ 9.1 H_2O/nm^2.

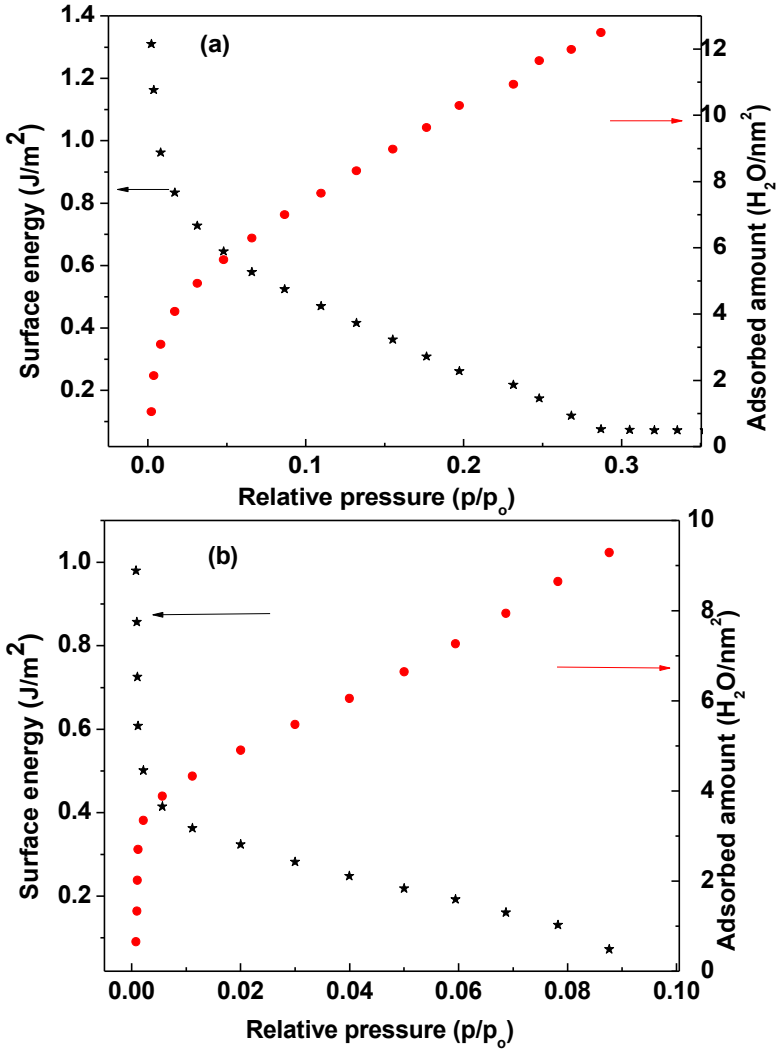

Figure 9. A plot of surface energy and surface water coverage as a function of relative pressure of water vapor on (a) $CeFCO_3$ and (b) $CaCO_3$

Implications for Ligand Design:

The enhancement in the beneficiation efficiency of bastnäsite relies on the design of collector molecules that are sufficiently selective for the REE-containing ore over calcite gangue. The most stable stoichiometric surfaces of bastnäsite ([$10\bar{1}0$]) and calcite ([$10\bar{1}4$]) are expected to be well expressed in their natural crystallites. The chemical environment around a metal ion is largely similar on these two surfaces, with carbonate as a common anion. On both surfaces, only

one water molecule coordinates to the metal ion directly. Furthermore, the adsorption energy of water molecules is approximately equal on these surfaces. Thus, as demonstrated for carboxylic acid based ligands,[2,5] collector molecules that bind to a single surface atom will be poorly selective for bastnäsite over calcite. Therefore, the design of floatation agents with enhanced selectivity for bastnäsite over calcite must exploit the structural differences in the predominantly exposed facets of these minerals. Along the two lattice directions, the metal ions are separated by 4.03 Å and 4.99 Å on the calcite [$10\bar{1}4$] surface, 4.80 Å and 7.07 Å on the La-bastnäsite [$10\bar{1}0$] surface, and 4.78 Å and 7.06 Å on the Ce-bastnäsite [$10\bar{1}0$] surface. Thus, ligands with two functional groups that are rigidly separated by *ca.* 7.1Å are expected to bind to bastnäsite preferentially over calcite, because the induced steric strain in the ligand resulting from coordination to two surface Ca^{2+} ions could render the binding less favorable. The close resemblance of surface structures and stabilities of Ce- and La-bastnäsite and the non-participation of the Ce *4f* electrons in bonding indicate that ligands designed for La-bastnäsite will be equally selective for Ce-bastnäsite over calcite. The results of this study provide the foundation for a rational design of collector molecules to achieve a significant improvement in flotation efficiency of REE-rich minerals. We are interested in designing hydroxamate and / or phosphonate based ligands that selectively bind to bastnäsite over calcite. The subsequent studies will focus on the adsorption of phosphinate and hydroxamate ligands on the Ce-bastnäsite [$10\bar{1}0$] surface to enable molecular design of collector molecules containing these donor groups.

Conclusions:

We have used a combination of density functional theory (DFT) and water adsorption calorimetry for a comparative study of crystal and electronic structure, surface and water

adsorption energies of Ce-bastnäsite, La-bastnäsite, and calcite. Ce- and La-bastnäsite are isomorphic materials, consisting of six formula units of $MFCO_3$ ($M = Ce^{3+}/La^{3+}$) in $P\bar{6}2c$ space group, arranged in two alternating layers of three MF^{2+} and three CO_3^{2-} groups. Spin polarized DFT+U calculations showed that the energy difference between different magnetic ordering of spins in Ce-bastnäsite is negligible, indicating minimal exchange interactions between the *4f* electrons on different Ce^{3+} ions. Similar to La-bastnäsite, Ce-bastnäsite is a wide band gap insulator. The valence and conduction band edges of Ce-bastnäsite predominantly consist of Ce 4*f* orbitals.

DFT calculations and calorimetry show higher surface energies and more favorable water adsorption energies on Ce-bastnäsite compared to La-bastnäsite surfaces, which is consistent with the smaller ionic radius and larger hydration enthalpy of the Ce^{3+} ions. Analysis of the electronic structure showed that the Ce f orbitals do not participate in bonding with the adsorbed water molecule, justifying the f-in-core pseudopotential approach in which the 4f electrons are incorporated into the pseudopotential. The structural features and the relative stability order of Ce- and La-bastnäsite surfaces are very similar, suggesting that Ce^{3+} and La^{3+} would be randomly distributed in natural bastnäsite samples forming solid solution. The adsorption energies of water molecules on the most stable surfaces of bastnäsite and calcite, namely $[10\bar{1}4]$ and $[10\bar{1}0]$, are nearly equal. Thus, rational design of collector molecules that are selective to bastnäsite over calcite must exploit the structural differences between the two materials.

Electronic Supplementary Information (ESI) Available: Geometric features of Ce-bastnäsite surfaces computed using the large-core pseudopotential, overlays of cleaved and optimized structures of Ce-bastnäsite and calcite surfaces, crystallographic information files containing optimized structures of the studied surfaces obtained from VASP calculations, and adsorption

isotherm for $CeFCO_3$ with corresponding calorimetric trace.

Author Information

Corresponding Authors

*(A.N.) E-mail: anavrotsky@ucdavis.edu, Tel: +1 530-752-3292

*(V.B.) E-mail: bryantsevv@ornl.gov, Tel: +1 865-576-4272

Notes

The authors declare no competing financial interest.

Acknowledgement

This work was supported by the Critical Materials Institute, an Energy Innovation Hub funded by the U.S. Department of Energy, Office of Energy Efficiency and Renewable Energy, Advanced Manufacturing Office. This research used resources of the Oak Ridge Leadership Computing Facility at the Oak Ridge National Laboratory, supported by the Office of Science of the U.S. Department of Energy under contract No. DE-AC05-00OR22725.

References

1. L. Meyer and B. Bras, presented in part at the 2011 IEEE International Symposium on Sustainable Systems and Technology (ISSST) 16-18 May, 2011.
2. A. Jordens, Y. P. Cheng and K. E. Waters, *Miner. Eng.*, 2013, **41**, 97-114.
3. N. Krishnamurthy and C. K. Gupta, *Extractive metallurgy of rare earths*, CRC press, 2004.
4. E. Alonso, A. M. Sherman, T. J. Wallington, M. P. Everson, F. R. Field, R. Roth and R. E. Kirchain, *Environ. Sci. Technol.*, 2012, **46**, 3406-3414.

5. D. W. Fuerstenau, *Miner. Metall. Process.*, 2013, **30**, 1-9.

6. S. B. Castor, *Can. Mineral.*, 2008, **46**, 779-806.

7. L. T. Peiro and G. V. Mendez, *JOM*, 2013, **65**, 1327-1340.

8. O. Pavez, P. R. G. Brandao and A. E. C. Peres, *Miner. Eng.*, 1996, **9**, 357-366.

9. J. Ren, S. Lu, S. Song and J. Niu, *Miner. Eng.*, 1997, **10**, 1395-1404.

10. Pradip and D. W. Fuerstenau, *Colloids. Surf.*, 1983, **8**, 103-119.

11. Pradip and D. W. Fuerstenau, *Colloids. Surf.*, 1985, **15**, 137-146.

12. Pradip and D. W. Fuerstenau, *Int. J. Miner. Process.*, 1991, **32**, 1-22.

13. J. Cui, G. A. Hope and A. N. Buckley, *Miner. Eng.*, 2012, **36–38**, 91-99.

14. S. M. Assis, L. C. M. Montenegro and A. E. C. Peres, *Miner. Eng.*, 1996, **9**, 103-114.

15. Pradip and B. Rai, *Int. J. Miner. Process.*, 2003, **72**, 95-110.

16. X. Zhang, H. Du, X. Wang and J. D. Miller, *Int. J. Miner. Process.*, 2014, **133**, 29-38.

17. S. G. Srinivasan, R. Shivaramaiah, P. R. C. Kent, A. G. Stack, A. Navrotsky, R. Riman, A. Anderko and V. S. Bryantsev, *J. Phys. Chem. C*, 2016, **120**, 16767-16781.

18. G. Kresse and J. Hafner, *Phys. Rev. B*, 1993, **47**, 558-561.

19. G. Kresse and J. Hafner, *Phys. Rev. B*, 1994, **49**, 14251-14269.

20. G. Kresse and J. Furthmüller, *Phys. Rev. B*, 1996, **54**, 11169-11186.

21. G. Kresse and J. Furthmüller, *Comput. Mater. Sci.*, 1996, **6**, 15-50.

22. P. E. Blöchl, *Phys. Rev. B*, 1994, **50**, 17953-17979.

23. G. Kresse and D. Joubert, *Phys. Rev. B*, 1999, **59**, 1758-1775.

24. J. P. Perdew, A. Ruzsinszky, G. I. Csonka, O. A. Vydrov, G. E. Scuseria, L. A. Constantin, X. Zhou and K. Burke, *Phys. Rev. Lett.*, 2008, **100**, 136406.

25. S. Grimme, J. Antony, S. Ehrlich and H. Krieg, *J. Chem. Phys*, 2010, **132**, 154104.

26. P. Pulay, *Chem. Phys. Lett.*, 1980, **73**, 393-398.

27. N. Hirosaki, S. Ogata and C. Kocer, *J. Alloy. Comp.*, 2003, **351**, 31-34.

28. M. Jinxiao, J. C. Shen, B. M. Pan and J. Liang, *Diqiu Kexue*, 1996, **21**, 63-67.

29. D. K. Smith and H. R. Leider, *J. Appl. Cryst.*, 1968, **1**, 246-249.

30. S. L. Dudarev, G. A. Botton, S. Y. Savrasov, C. J. Humphreys and A. P. Sutton, *Phys. Rev. B*, 1998, **57**, 1505-1509.

31. B. Meredig, A. Thompson, H. A. Hansen, C. Wolverton and A. van de Walle, *Phys. Rev. B*, 2010, **82**, 195128.

32. J. W. Anthony, R. A. Bideaux, K. W. Bladh and M. C. Nichols, *Handbook of mineralogy, mineralogical society of America, Chantilly, VA 20151-1110, USA*, 2011.

33. G. Makov and M. C. Payne, *Phys. Rev. B*, 1995, **51**, 4014-4022.

34. J. Neugebauer and M. Scheffler, *Phys. Rev. B*, 1992, **46**, 16067-16080.

35. G. Z. Wulff, *Z. Kristallogr,* 1901, **34**, 449-530.

36. R. V. Zucker, D. Chatain, U. Dahmen, S. Hagege and W. C. Carter, *J. Mater. Sci.*, 2012, **47**, 8290-8302.

37. Wulffman software, http://www.ctcms.nist.gov/wulffman/.

38. K. Mathew, R. Sundararaman, K. Letchworth-Weaver, T. A. Arias and R. G. Hennig, *J. Chem. Phys*, 2014, **140**, 084106.

39. K. Momma and F. Izumi, *J. Appl. Cryst.*, 2011, **44**, 1272-1276.

40. G. Donnay and J. Donnay, *Am. Mineral.*, 1953, **38**, 932-963.

41. R. Shivaramaiah, A. Anderko, R. E. Riman and A. Navrotsky, *Am. Mineral.*, 2016, **101**, 1129-1134.

42. R. H. R. Castro and D. V. Quach, *J. Phys. Chem. C,* 2012, **116**, 24726-24733.

43. J. W. Drazin and R. H. R. Castro, *J. Phys. Chem. C,* 2014, **118**, 10131-10142.

44. H. Effenberger, K. Mereiter and J. Zemann, *Z. Kristallogr.*, 1981, **156**, 233-244.

45. D. Waeman, W. H. Evans, V. Paskes, R. Schumm, S. Bailey and I. Halow, *J. Phys. Chem. Ref. Data*, 1982, **11**.

46. D. R. Baer and D. L. Blanchard, *Appl. Surf. Sci.*, 1993, **72**, 295-300.

47. S. Lutfalla, V. Shapovalov and A. T. Bell, *J. Chem. Theory Comput.*, 2011, **7**, 2218-2223.

48. S. Fabris, S. de Gironcoli, S. Baroni, G. Vicario and G. Balducci, *Phys. Rev. B*, 2005, **72**, 237102.

49. W. Q. Li, S. Goverapet Srinivasan, D. R. Salahub and T. Heine, *Phys Chem Chem Phys*, 2016, **18**, 11139-11149.

50. Y.-Q. Su, I. A. W. Filot, J.-X. Liu, I. Tranca and E. J. M. Hensen, *Chem. Mater.*, 2016, **28**, 5652-5658.

51. M. Capdevila-Cortada and N. Lopez, *Nat Mater*, 2016, Doi:10.1038/nmat4804.

52. C. Noguera, *J. Phys.: Condens. Matter*, 2000, **12**, R367.

53. R. D. Shannon and C. T. Prewitt, *Acta Crystallogr., Sect B*, 1970, **26**, 1046-1048.

54. Y. Marcus, *Ion properties*, Marcel Dekker, Inc., 1997.

55. Bastnäsite-(Ce), http://www.mindat.org/min-560.html.

56. N. H. de Leeuw and S. C. Parker, *J. Phys. Chem. B*, 1998, **102**, 2914-2922.

57. P. Fenter, S. Kerisit, P. Raiteri and J. D. Gale, *J. Phys. Chem. C*, 2013, **117**, 5028-5042.

58. J. Narbutt, A. Wodynski and M. Pecul, *Dalton Trans.*, 2015, **44**, 2657-2666.

59. J. S. Lardge, D. M. Duffy and M. J. Gillan, *J. Phys. Chem. C*, 2009, **113**, 7207-7212.

60. D. Addari and A. Satta, *J. Phys. Chem. C*, 2015, **119**, 19780-19788.

61. A. Navrotsky, *Int. J. Quant. Chem*. 2009, **109**, 2648-2657.

Graphical Abstract:

Rational design of collector molecules that are selective to bastnäsite over calcite must exploit the structural differences between the two materials

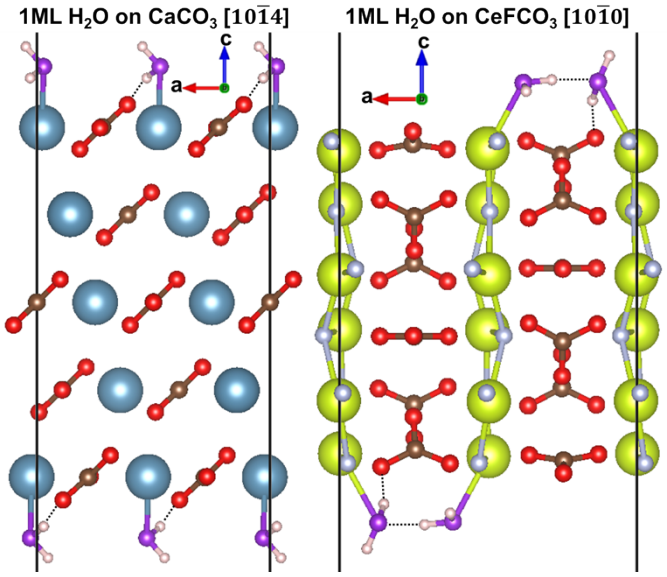

Table 2: C-O and Ce-F bond lengths in Ce-bastnäsite and C-O bond lengths in calcite.[a]

Structure	r_{C-O}^{min} (Å)	r_{C-O}^{max} (Å)	r_{C-O}^{avg} (Å)	r_{Ce-F}^{min} (Å)	r_{Ce-F}^{max} (Å)	r_{Ce-F}^{avg} (Å)	Δ_{C-O} (%)	Δ_{Ce-F} (%)	δ_{C-O}(%)	δ_{Ce-F}(%)
Ce – Bastnäsite using full valence pseudopotential										
bulk	1.289	1.292	1.291	2.393	2.403	2.397	0	0	0.26	0.39
$[10\bar{1}0]$-(a)	1.275	1.313	1.291	2.290	2.452	2.382	0.05	-0.60	2.89	6.82
$[10\bar{1}0]$-(b)	1.277	1.326	1.291	2.288	2.472	2.382	0.03	-0.63	3.79	7.72
$[10\bar{1}1]$–CO_3^{2-}	1.258	1.344	1.294	2.247	2.569	2.388	0.25	-0.39	6.63	13.45
$[10\bar{1}1]$ –Ce^{3+}	1.259	1.350	1.295	2.247	2.562	2.395	0.29	-0.10	7.03	13.17
$[10\bar{1}1]$–F^-	1.246	1.364	1.295	2.085	2.599	2.382	0.34	-0.60	9.10	21.55
$[10\bar{1}1]$–CeF^{2+}	1.267	1.345	1.294	2.239	2.578	2.389	0.22	-0.35	6.08	14.21
$[10\bar{1}1]$–$CeFCO_3$	1.263	1.352	1.295	2.221	2.573	2.387	0.29	-0.42	6.88	14.76
$[10\bar{1}2]$	1.257	1.355	1.293	2.276	2.489	2.394	0.20	-0.14	7.53	8.92
[0001]– CO_3^{2-}	1.254	1.392	1.297	2.300	2.563	2.427	0.49	1.27	10.63	10.83
[0001]–CeF^{2+}	1.254	1.361	1.295	2.100	2.433	2.349	0.33	-1.98	8.22	14.19
$[11\bar{2}2]$	1.239	1.356	1.296	2.277	2.587	2.356	0.40	-1.73	9.01	13.13
$[10\bar{1}4]$	1.211	1.427	1.295	2.296	2.588	2.412	0.33	0.63	16.70	12.10
Calcite										
bulk	1.293	1.293	1.293	-	-	-	0	-	0	-
$[10\bar{1}4]$	1.273	1.313	1.294	-	-	-	0.02	-	3.06	-

[a]The percentage change in the average C–O and Ce–F bond lengths with respect to the bulk, Δ_{C-O} and Δ_{Ce-F} , is calculated using equation (3). The percentage of spread in the C–O and Ce–F bond lengths with respect to the average C–O and Ce–F bond lengths in each structure, δ_{C-O} and $\delta_{Ce-F,}$ is calculated using equation (4).

Table 3: Surface and solvation energies of bastnäsite.

Surface	#$MFCO_3$ formula units[b]	Slab Thickness (Å)	Symmetry	E^{vac}_{surf}(J/m^2)			E^{sol}(J/m^2)		E^{surf}(J/m^2)	
				$CeFCO_3$		$LaFCO_3$ [a]	$CeFCO_3$ f-in-core	$LaFCO_3$ [a]	$CeFCO_3$ *f*-in-core	$LaFCO_3$ [a]
				f-in-core	*f*-in-valence					
$[10\bar{1}0]$-(a)	14	14.77	*Pma2*	0.79	0.76	0.73	-0.31	-0.27	0.48	0.45
$[10\bar{1}0]$-(b)	12	10.81	*Pmn2$_1$*	0.84	0.82	0.77	-0.30	-0.28	0.54	0.49
$[10\bar{1}1]$–CO_3^{2-}	24	11.95	P_1	0.96	0.92	0.89	-0.37	-0.33	0.59	0.56
$[10\bar{1}1]$ –M^{3+} [b]	24	11.46	P_1	1.06	1.01	0.99	-0.39	-0.35	0.67	0.64
$[10\bar{1}1]$–F^-	24	11.46	P_1	1.21	1.15	1.11	-0.46	-0.40	0.75	0.71
$[10\bar{1}1]$–MF^{2+} [b]	24	11.73	P_1	1.02	0.99	0.95	-0.40	-0.36	0.62	0.59
$[10\bar{1}1]$–$MFCO_3$[b]	24	12.05	P_1	1.09	1.04	1.01	-0.42	-0.38	0.67	0.63
$[10\bar{1}2]$	18	13.64	P_2	1.11	1.06	1.03	-0.40	-0.35	0.71	0.68
[0001]– CO_3^{2-}	12	12.02	P_m	1.16	1.12	1.09	-0.28	-0.26	0.88	0.83
[0001]–MF^{2+} [b]	12	10.82	P_2	1.20	1.17	1.10	-0.40	-0.35	0.80	0.75
$[11\bar{2}2]$	24	10.81	P_1	1.30	1.20	1.18	-0.46	-0.40	0.84	0.78
$[10\bar{1}4]$	30	12.89	P_2	1.43	1.37	1.35	-0.47	-0.43	0.96	0.92

[a]Values taken from Ref. 17

[b]M = Ce for $CeFCO_3$ and M = La for $LaFCO_3$

Table 4: Surface and solvation energy of calcite.

Surface	#$CaCO_3$ formula units	Slab Thickness (Å)	Symmetry	E^{vac}_{surf}(J/m^2)	E^{sol}(J/m^2)	E^{surf}(J/m^2)
$[10\bar{1}4]$	10	13.57	*P6/2c*	0.59	-0.32	0.27